Simulation and Reynolds-averaged Navier-Stokes modeling of a three-component Rayleigh-Taylor mixing problem with thermonuclear burn

Brandon E. Morgan
Lawrence Livermore National Laboratory, Livermore, California 94550, USA

(Received 8 November 2021; accepted 30 March 2022; published 14 April 2022)

Rayleigh-Taylor mixing in the presence of a third component with intermediate density is investigated through three-dimensional large-eddy simulation (LES) with a high-order compact finite-difference code. Two configurations are considered: (1) a symmetric configuration in which the Atwood number between the heavy and intermediate components matches the Atwood number between the intermediate and light components and (2) an asymmetric configuration in which the Atwood number between the heavy and intermediate components is an order of magnitude greater than the Atwood number between the intermediate and light components. Mass fraction covariances are extracted, and proposed Reynolds-averaged Navier-Stokes (RANS) closures for density-specific-volume and density-mass-fraction covariances are evaluated in an *a priori* fashion. In addition, a multicomponent extension of the $k-\phi-L-a-V$ RANS model [Morgan, Phys. Rev. E **104**, 015107 (2021)] is presented which includes model equations for the upper-triangular elements of the mass fraction covariance matrix. This model, referred to as the $k-\phi-L-a-\mathcal{C}$ model, is compared against results from LES and against other RANS models. Profiles of average mass fraction, mass-fraction covariance, and density-specific-volume covariance obtained with the $k-\phi-L-a-\mathcal{C}$ model are found to agree well with LES data. Finally, the impact of three-component turbulent mixing on average reaction rate is investigated in both premixed and nonpremixed cases by heating the mixing layer and allowing it to undergo thermonuclear (TN) burn. A closure model for average reaction rate is proposed for use with the $k-\phi-L-a-\mathcal{C}$ model, and when this model is applied, improved agreement is obtained between LES and RANS in total TN neutron production.

DOI: 10.1103/PhysRevE.105.045104

I. INTRODUCTION

Turbulent mixing layers are encountered in a variety of physical systems, including oceanic and atmospheric flows [1–4], astrophysical phenomena [5], and in applications of inertial confinement fusion (ICF) [6,7]. When such mixing occurs in the context of reacting turbulence, whether the reactions are chemical or nuclear in nature, accurate prediction of the statistics of scalar transport are vital to understanding the impact of turbulence on reaction rate. [8,9].

In classical Rayleigh-Taylor (RT) mixing, two fluids mix when they are subject to an acceleration gradient that is opposite in direction to the mean density gradient [10,11]. For problems of two-fluid mixing, second-moment statistics of a passive scalar can be characterized with a single scalar variance [9,12]. In practical problems of engineering interest, however, it is frequently the case that more than two components will be involved in the mixing process. In the "CD Symcap" ICF experiments, for example, tritium-filled capsules were surrounded by a silicon-doped plastic ablator (CH), and a deuterated plastic (CD) layer was either placed against the tritium gas or recessed within the ablator by up to 8 μm [13,14]. In problems such as this, a single scalar variance is not sufficient to fully describe the multicomponent mixing process that occurs between the gas, the CD plastic, and the surrounding plastic ablator which acts as a nonreacting contaminant.

To better understand the physics of mixing when more than two materials are involved, the present work considers the case of a three-component RT mixing layer in which the heavy material is initially separated from light material by the presence of a third, intermediate-density material. All three materials are subject to an acceleration gradient such that interfaces between heavy and intermediate and between intermediate and light components both become unstable, and eventually the heavy material penetrates through the intermediate material to mix directly with the light material. Figure 1 illustrates schematically the three-component RT mixing problem under consideration, where ρ indicates density and subscripts 1, 2, and 3 refer to the light, intermediate, and heavy mixing components, respectively, such that $\rho_1 < \rho_2 < \rho_3$. In the late-time limit of this problem, the intermediate material becomes negligibly diffuse, and the problem reduces to a classical two-component RT mixing layer between the heavy and light components. The present work therefore considers mixing behavior prior to this late-time limit, when the presence of the intermediate material is still observable and significant.

Reacting Rayleigh-Taylor turbulence has been investigated previously in classical two-component configurations [9,15,16]. The present work builds on these prior works by considering the impact of an additional inert contaminant material. First, high-fidelity large-eddy simulation (LES) is performed of the nonreacting three-component RT problem

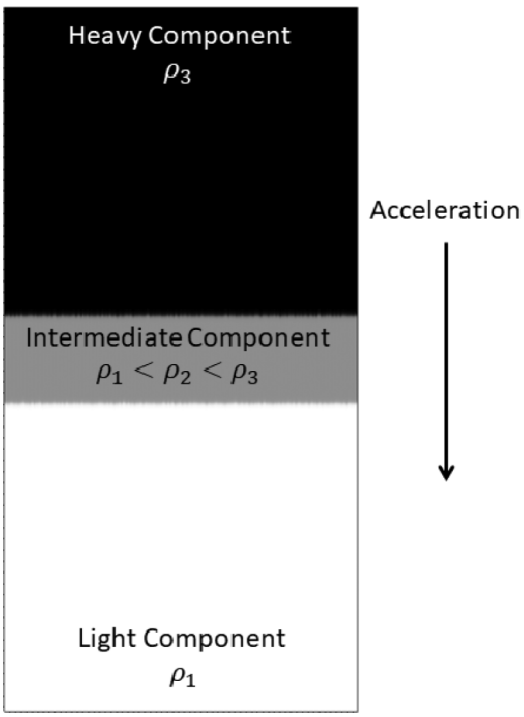

FIG. 1. Schematic representation of the three-component RT mixing problem under consideration. Simulations include premixed and nonpremixed reactant cases as well as symmetric and asymmetric Atwood number configurations.

with the high-order finite-difference code *Miranda*. Two configurations are considered, which can be described by the general Atwood number,

$$A_{ij} \equiv \frac{\rho_i - \rho_j}{\rho_i + \rho_j}. \tag{1}$$

A symmetric configuration is considered in which $A_{32} = A_{21}$, and an asymmetric configuration is considered in which $A_{32} = 10 \times A_{21}$. In each case, the mixing layer is allowed to evolve until there is significant interpenetration of the heavy component into the light component. Then, the mixing layer is heated to 10 keV, and thermonuclear (TN) burn is initiated. Both premixed and nonpremixed configurations are considered. In the premixed configuration, the intermediate material is considered to be a mixture of deuterium (D) and tritium (T) gas, while the heavy and light components are taken to be inert plastics (CH). In the nonpremixed configuration, the intermediate material is taken to be CH, while the light material is treated as T, and the heavy material is treated as deuterated plastic (CD).

Since Reynolds-averaged Navier-Stokes (RANS) modeling remains a common tool in ICF design and analysis, RANS simulation of the three-component RT mixing problem is also considered. Recently, the $k - \phi - L - a - V$ RANS model has been developed for the simulation of two-fluid turbulent mixing [12]. The $k - \phi - L - a - V$ model represents an improvement over similar models that assume a linear mixing profile and quadratic turbulence profiles [9,17–21]. In contrast, the $k - \phi - L - a - V$ model relaxes the assumption of a linear mixing profile and admits self-consistent high-order spatial profiles through similarity analysis [12]. By design, however, the $k - \phi - L - a - V$ model and other models that transport a single mass fraction variance rely on an assumption of only two mixing components. Similarly, existing models for the impact of turbulent mixing on average TN reaction rate [9,22] have been formulated under the same assumption of two-component mixing. Thus, a need exists to extend these models in order to perform RANS simulation of the three-component mixing layer under consideration. To this end, an extension of the $k - \phi - L - a - V$ model, referred to as the $k - \phi - L - a - \mathcal{C}$ model, is presented which solves transport equations for the upper triangular elements of the mass fraction covariance matrix. These mass fraction covariances are then utilized to construct a general model for the impact of turbulent mixing on reaction rate, and one-dimensional (1D) RANS results using these models are shown to agree well with high-fidelity LES.

The remainder of this paper is laid out as follows. First, in Sec. II, the numerical models utilized in the present work are presented. Descriptions of the *Miranda* and *Ares* computational codes are given in Sec. II A, and the $k - \phi - L - a - \mathcal{C}$ model is introduced in Sec. II B. Then, in Secs. II C and II D, detailed descriptions are given of the computational setup of the three-component RT problem for LES and RANS simulations. Results are presented in Sec. III, focusing first on the initial nonreacting growth phase of the simulations in Sec. III A followed by comparisons between RANS and LES during the reacting phase of simulations in Sec. III B. Finally, in Sec. IV conclusions are drawn, and recommendations are made regarding the direction of future research.

II. NUMERICAL MODELS

A. Computational codes

Three-dimensional LES calculations in the present work are solved in two stages. First, the *Miranda* code is used to evolve the nonreacting layer until it is well mixed and turbulent. Then, in a second stage of simulation, the mixing layer is heated, and the *Ares* code is used to further evolve the mixing layer as it undergoes TN burn with coupled radiation diffusion. This approach has been used previously in simulations of a reacting, two-component RT mixing layer in a spherical geometry [9].

The *Miranda* code solves the compressible Navier-Stokes equations presented in Appendix 1 with a 10th-order compact differencing scheme for spatial discretization and a 4th-order explicit Runge-Kutta scheme for temporal integration. *Miranda* has been utilized extensively in previous studies of compressible turbulent mixing [20,23–33]. To model the subgrid scale transfer of energy, *Miranda* utilizes an artificial fluid LES approach in which artificial transport terms are added to the fluid viscosity, the bulk viscosity, the thermal conductivity, and the molecular diffusivity [34,35]. The form of the artificial contributions utilized in the present work is the same as that utilized in earlier work by Morgan *et al.* [9]. Since the present study is focused on the high-Reynolds-number regime in which viscous length scales are significantly smaller than energy-containing structures, the approach of Olson *et al.* [26] is adopted, and fluid contributions to dynamic viscosity,

TABLE I. Summary of TN reactions supported by *Ares*.

No.	reaction	$Q_{\rm TN}$ (MeV)
1	$\mathrm{D}+\mathrm{D}\rightarrow n^0+{}^3\mathrm{He}$	3.26
2	$\mathrm{D}+\mathrm{D}\rightarrow {}^1\mathrm{H}+\mathrm{T}$	4.02
3	$\mathrm{T}+\mathrm{T}\rightarrow n^0+n^0+{}^4\mathrm{He}$	11.32
4	$\mathrm{D}+\mathrm{T}\rightarrow n^0+{}^4\mathrm{He}$	17.59
5	$\mathrm{D}+{}^3\mathrm{He}\rightarrow {}^1\mathrm{H}+{}^4\mathrm{He}$	18.35

bulk viscosity, thermal conductivity, and molecular diffusivity are taken to be zero (i.e., $\mu_f=\beta_f=\kappa_f=D_{f,k}=0$). This modeling choice represents a trade-off between resolution of the finest scales and development of the inertial range. By relying on hyperdiffusivity to capture mixing at the finest scales, the present simulations allow for the maximal separation of scales possible under the computational framework and enable simulation of mixing in a fully turbulent, self-similar state. Since the comparison RANS simulations assume a self-similar state, the choice to neglect physical contributions to viscosity and diffusivity facilitates the most direct comparison between RANS and LES. While this means that the finest scales of mixing in the LES results are governed by artificial diffusive terms, the integral mixing behavior has been shown to be well captured, including in problems of reacting flow [9,30].

The *Ares* code solves the hydrodynamics equations in Appendix 1 coupled with a radiation diffusion approach presented in Appendix 2. *Ares* uses an arbitrary Lagrangian-Eulerian method with a second-order remap [36]. Explicit time integration is accomplished with a second-order predictor-corrector scheme [37], and spatial differences are computed with a nondissipative second-order finite-element approach. A tensor artificial viscosity [38] is applied for the capturing of shocks and material discontinuities. Although *Ares* also boasts an adaptive mesh refinement capability [39,40], it is not utilized in the present study. *Ares* has been applied previously in studies of canonical Richtmyer-Meshkov instability in both planar [28] and cylindrical [41] configurations. It has also been utilized extensively in the simulation of ICF targets and experiments [13,42–48].

In the present work, five TN reactions are computed by *Ares*, as summarized by Table I. In these reactions, products can be either neutrons, indicated by n^0, or charged particles. The rate of a given reaction with products γ and reactants α and β is given simply by

$$\dot{r}_{\gamma,\alpha\beta}=\langle\sigma v\rangle_{\alpha\beta}n_\alpha n_\beta, \tag{2}$$

where $\langle\sigma v\rangle_{\alpha\beta}$ is the reaction cross section, and n_α and n_β are the particle number densities. The reaction cross section is interpolated using the TDFv2.3 library [49]. Additionally, each reaction has an average thermal energy $Q_{\rm TN}$, which is tabulated in Table I. Local deposition of this energy is assumed such that the average thermal energy is removed from the ion energy field, and charged particle energy is deposited in the same volume with a split between the ion and electron energies according to the Corman-Spitzer model [50]. Neutrons are assumed to immediately escape the problem, and energy carried by neutron products is removed from the system. Thermal effects and the apportionment of average thermal energy among reactants are determined following the method by Warshaw [49]. Additionally, the ion-electron coupling coefficient K_{ie} is determined according to Brysk [51].

B. The $k-\phi-L-a-\mathcal{C}$ model

The $k-\phi-L-a-\mathcal{C}$ model is a multicomponent extension of the $k-\phi-L-a-V$ model [12]. In the present work, an overbar denotes Reynolds averaging and a tilde denotes mass-weighted (Favre) averaging. An arbitrary scalar, f, is decomposed as

$$f=\overline{f}+f'=\widetilde{f}+f'', \tag{3}$$

where the Favre average is related to the Reynolds average according to

$$\widetilde{f}=\frac{\overline{\rho f}}{\overline{\rho}}. \tag{4}$$

The Reynolds stress tensor, mass-flux velocity vector, density–specific-volume covariance, and mass fraction covariances are defined, respectively, in terms of the velocity vector, u_i, the specific volume, $1/\rho$, and the component mass fraction, Y_α, by

$$\overline{\rho}\tau_{ij}\equiv-\overline{\rho u_i'' u_j''}, \tag{5a}$$

$$a_i\equiv-\overline{u_i''}, \tag{5b}$$

$$b\equiv-\overline{\rho'\left(\frac{1}{\rho}\right)'}, \tag{5c}$$

$$\mathcal{C}_{\alpha\beta}\equiv\widetilde{Y_\alpha''Y_\beta''}. \tag{5d}$$

Equations (6)–(20) below summarize the $k-\phi-L-a-\mathcal{C}$ model, where v is the volume fraction, μ_t is the eddy viscosity, g_j is the gravitational acceleration vector, e is the specific internal energy, ϕ is the turbulent velocity, L is the turbulent length scale, N is the total number of mixing components, and V is half the trace of the mass fraction covariance matrix. The model coefficients C_A, C_B, C_D, C_{p1}, C_{p2}, C_{p3}, C_{L1}, C_{L2}, C_{L3}, C_{C1}, C_{C2}, C_{C3}, N_a, N_e, N_k, N_p, N_L, N_C, N_Y, and $C_{\rm dev}$ are determined through similarity analysis. The model equations are

$$\frac{D\overline{\rho}}{Dt}=-\overline{\rho}\frac{\partial\widetilde{u}_i}{\partial x_i}, \tag{6}$$

$$\overline{\rho}\frac{D\widetilde{Y}_\alpha}{Dt}=\frac{\partial}{\partial x_i}\left(\frac{\mu_t}{N_Y}\frac{\partial\widetilde{Y}_\alpha}{\partial x_i}\right)+\overline{\dot{r}}_\alpha, \tag{7}$$

$$\overline{\rho}\frac{D\widetilde{u}_j}{Dt}=\overline{\rho}g_j-\frac{\partial\overline{p}}{\partial x_j}+\frac{\partial}{\partial x_i}(\overline{\rho}\tau_{ij}), \tag{8}$$

$$\overline{\rho}\frac{D\widetilde{e}}{Dt}=-\overline{p}\frac{\partial\widetilde{u}_i}{\partial x_i}-a_i\frac{\partial\overline{p}}{\partial x_i}+C_D\frac{\overline{\rho}\phi k}{L}+\frac{\partial}{\partial x_i}\left(\frac{\mu_t}{N_e}\frac{\partial\widetilde{e}}{\partial x_i}\right), \tag{9}$$

$$\overline{\rho}\frac{Dk}{Dt}=\overline{\rho}\tau_{ij}\frac{\partial\widetilde{u}_i}{\partial x_j}+a_i\frac{\partial\overline{p}}{\partial x_i}-C_D\frac{\overline{\rho}\phi k}{L}+\frac{\partial}{\partial x_i}\left(\frac{\mu_t}{N_k}\frac{\partial k}{\partial x_i}\right), \tag{10}$$

$$\overline{\rho}\frac{D\phi}{Dt}=C_{p1}\overline{\rho}\frac{\phi^2}{L}+C_{p2}\frac{1}{\phi V^{3/8}}\overline{\rho}\tau_{ij}\frac{\partial\widetilde{u}_i}{\partial x_j}+C_{p3}\frac{a_i}{\phi V^{3/8}}\frac{\partial\overline{p}}{\partial x_i}+\frac{\partial}{\partial x_i}\left(\frac{\mu_t}{N_p}\frac{\partial\phi}{\partial x_i}\right), \tag{11}$$

$$\overline{\rho}\frac{DL}{Dt} = C_{L1}\overline{\rho}\phi + C_{L2}\overline{\rho}L\frac{\partial\widetilde{u}_i}{\partial x_i} + C_{L3}\overline{\rho}\tau_{ij}\frac{L}{k}\frac{\partial\widetilde{u}_i}{\partial x_j} + \frac{\partial}{\partial x_i}\left(\frac{\mu_t}{N_L}\frac{\partial L}{\partial x_i}\right), \tag{12}$$

$$\overline{\rho}\frac{Da_j}{Dt} = C_B\frac{b}{V^{3/8}}\frac{\partial\overline{p}}{\partial x_j} - C_A\overline{\rho}\frac{\phi}{L}a_j + \frac{\tau_{ij}}{V^{3/8}}\frac{\partial\overline{\rho}}{\partial x_i} + \frac{\partial}{\partial x_i}\left(\frac{\mu_t}{N_a}\frac{\partial a_j}{\partial x_i}\right), \tag{13}$$

$$\overline{\rho}\frac{D\mathcal{C}_{\alpha\beta}}{Dt} = C_{C1}\mu_t\frac{\partial\widetilde{Y}_\alpha}{\partial x_i}\frac{\partial\widetilde{Y}_\beta}{\partial x_i} - C_{C2}\overline{\rho}\frac{\phi}{L}\mathcal{C}_{\alpha\beta} + C_{C3}\mathcal{C}_{\alpha\beta}\frac{a_i}{k}\frac{\partial\overline{p}}{\partial x_i} + \frac{\partial}{\partial x_i}\left(\frac{\mu_t}{N_C}\frac{\partial\mathcal{C}_{\alpha\beta}}{\partial x_i}\right), \tag{14}$$

where

$$\frac{D}{Dt} \equiv \frac{\partial}{\partial t} + \widetilde{u}_i\frac{\partial}{\partial x_i}, \tag{15}$$

$$\mu_t = \overline{\rho}L\phi, \tag{16}$$

$$\widetilde{S}_{ij} = \frac{1}{2}\left(\frac{\partial\tilde{u}_i}{\partial x_j} + \frac{\partial\tilde{u}_j}{\partial x_i}\right) - \frac{1}{3}\frac{\partial\tilde{u}_k}{\partial x_k}\delta_{ij}, \tag{17}$$

$$\overline{\rho}\tau_{ij} = C_{\rm dev}2\mu_t\widetilde{S}_{ij} - \tfrac{2}{3}\overline{\rho}k\delta_{ij}, \tag{18}$$

$$V = \sum_{\alpha=1}^{N-1}\sum_{\beta=\alpha+1}^{N} -\mathcal{C}_{\alpha\beta}, \tag{19}$$

and

$$b = -\sum_{\alpha=1}^{N-1}\sum_{\beta=\alpha+1}^{N}\left(\frac{\overline{v}_\alpha}{\widetilde{Y}_\alpha} - \frac{\overline{v}_\beta}{\widetilde{Y}_\beta}\right)^2\mathcal{C}_{\alpha\beta}. \tag{20}$$

Since the mass fraction covariance matrix is symmetric, and mass fractions are constrained to sum to unity, only upper diagonal components need to be transported according to Eq. (14). So, for instance, in a problem involving three mixing components, only the $\mathcal{C}_{12}$, $\mathcal{C}_{13}$, and $\mathcal{C}_{23}$ components need to be transported. Remaining diagonal components of the mass fraction covariance matrix can be derived according to

$$\mathcal{C}_{\alpha\alpha} = \sum_{\beta=1,\beta\neq\alpha}^{N} -\mathcal{C}_{\alpha\beta}. \tag{21}$$

Similarly, in a problem with only two mixing components, only a single covariance component needs to be transported ($\mathcal{C}_{12}$), and the $k-\phi-L-a-\mathcal{C}$ model reduces to the $k-\phi-L-a-V$ model.

TABLE II. Summary of physical parameters used to constrain $k-\phi-L-a-\mathcal{C}$ model coefficients.

α	$\Theta_{\rm RT}$	n	m	Φ^{-1}	$\delta/\mathcal{A}$	$\Theta_{\rm KH}$
0.03	0.80	1.11	1.33	0.035	0.08	0.80

Model coefficients are set through similarity analysis in a procedure identical to that outlined for the $k-\phi-L-a-V$ model [12] in terms of the RT growth parameter α, the RT mixedness $\Theta_{\rm RT}$, the mechanical decay exponent for homogeneous isotropic turbulence (HIT) n, the scalar decay exponent for HIT m, the Kelvin-Helmholtz (KH) turbulence intensity Φ^{-1}, the KH growth parameter $\delta/\mathcal{A}$, and the KH mixedness $\Theta_{\rm KH}$. More complete description of these parameters is given by Morgan [12], but the values of these parameters used to set model coefficients in the present work are given in Table II. Table III then summarizes the full set of model coefficients used.

To close the average reaction rate, the expression $m_\alpha n_\alpha = \rho Y_\alpha$ is utilized to transform Eq. (2) to the following form in terms of the species molar mass m_α:

$$\dot{r}_{\gamma,\alpha\beta} = \frac{\langle\sigma v\rangle_{\alpha\beta}Y_\alpha Y_\beta\rho^2}{m_\alpha m_\beta}. \tag{22}$$

Then, by applying a Reynolds decomposition and averaging, Eq. (22) is transformed into

$$\overline{\dot{r}_{\gamma,\alpha\beta}} = \frac{\langle\sigma v\rangle_{\alpha\beta}\widetilde{Y}_\alpha\widetilde{Y}_\beta\overline{\rho}^2}{m_\alpha m_\beta} \times\left\{1 + \frac{\widetilde{Y''_\alpha Y''_\beta}}{\widetilde{Y}_\alpha\widetilde{Y}_\beta} + \frac{\overline{\rho'\rho'}}{\overline{\rho}^2} + \frac{\overline{\rho' Y''_\alpha}}{\overline{\rho}\widetilde{Y}_\alpha} + \frac{\overline{\rho' Y''_\beta}}{\overline{\rho}\widetilde{Y}_\beta} + \text{h.o.t.}\right\}, \tag{23}$$

where fluctuations of the cross section have been neglected, and third- and fourth-order moments have been indicated by the abbreviation h.o.t. (high-order terms). To close the density-mass-fraction covariance terms in Eq. (23), the following relationship is proposed:

$$\frac{\overline{\rho' Y''_\alpha}}{\overline{\rho}} \approx \sum_{\beta=1}^{N}\left(\frac{\overline{v}_\alpha}{\widetilde{Y}_\alpha} - \frac{\overline{v}_\beta}{\widetilde{Y}_\beta}\right)\mathcal{C}_{\alpha\beta}\,. \tag{24}$$

Then, assuming that the turbulent density intensity $\overline{\rho'\rho'}/\overline{\rho}^2$ can be approximated by the previous expression for b, substituting back into Eq. (23) gives the reaction rate closure,

$$\overline{\dot{r}_{\gamma,\alpha\beta}} \approx \frac{\langle\sigma v\rangle_{\alpha\beta}\widetilde{Y}_\alpha\widetilde{Y}_\beta\overline{\rho}^2}{m_\alpha m_\beta}\left[1 + \frac{\mathcal{C}_{\alpha\beta}}{\widetilde{Y}_\alpha\widetilde{Y}_\beta} - \sum_{i=1}^{N-1}\sum_{j=i+1}^{N}\left(\frac{\overline{v}_i}{\widetilde{Y}_i} - \frac{\overline{v}_j}{\widetilde{Y}_j}\right)^2\mathcal{C}_{ij} + \sum_{j=1}^{N}\left(\frac{\overline{v}_\alpha}{\widetilde{Y}_\alpha} - \frac{\overline{v}_j}{\widetilde{Y}_j}\right)\frac{\mathcal{C}_{\alpha j}}{\widetilde{Y}_\alpha} + \sum_{j=1}^{N}\left(\frac{\overline{v}_\beta}{\widetilde{Y}_\beta} - \frac{\overline{v}_j}{\widetilde{Y}_j}\right)\frac{\mathcal{C}_{\beta j}}{\widetilde{Y}_\beta}\right]. \tag{25}$$

Equation (25) is general for both premixed or nonpremixed reactants. In the *Ares* code, a simplification is made by grouping reactants into *materials*. For example, in the present problem D and T are considered reactants while more generally gas and plastic are considered materials. Thus, reactants may be initially premixed, as in a DT gas material mixing with CH plastic material, or nonpremixed, as in T gas material mixing with CD deuterated plastic material. An assumption is then

TABLE III. Model coefficients for the $k-\phi-L-a-\mathcal{C}$ model.

$C_{\rm dev}$	C_B	C_D	C_{L1}	C_{L2}	C_{L3}	C_{p1}	C_{p2}	C_{p3}	C_A	C_{C1}	C_{C2}	C_{C3}	$N_{Y,e,k,a}$	$N_{L,p}$	N_C
12.0	0.242	1.00	0.400	0.472	0.208	-0.500	6.89×10^{-4}	0.0576	1.286	15.3	1.20	0.352	0.119	0.0238	0.190

made that fluctuations of reactant mass fractions can be related to fluctuations of the material mass fraction. For instance, if reactant α is in the material 1, then it is assumed,

$$\frac{Y_\alpha''}{\widetilde{Y}_\alpha} \approx \frac{Y_1''}{\widetilde{Y}_1}. \tag{26}$$

For reactions among premixed reactants in the same material, Eq. (21) can be substituted to evaluate the first covariance term on the right-hand side of Eq. (25).

C. LES problem setup and initial conditions

Three-dimensional LES calculations are conducted on a computational mesh of dimension $2\pi\times2\pi\times4\pi$ cm^3 with the gravitational acceleration vector oriented in the negative z dimension. The initial thickness of the intermediate-density material is taken to be $1/8$ of the domain size in z, such that the light material is initialized with ρ_1 from $-2\pi\leqslant z<-\frac{\pi}{4}$, the intermediate-density material is initialized with ρ_2 from $-\frac{\pi}{4}\leqslant z<\frac{\pi}{4}$, and the heavy material is initialized with ρ_3 from $\frac{\pi}{4}\leqslant z\leqslant 2\pi$. Fluid densities are chosen such that $\rho_3=0.01$ g/cm^3, and other component densities are determined based on desired Atwood numbers. Table IV summarizes material densities and Atwood numbers for the two configurations considered. In the symmetric configuration, $A_{32}=A_{21}$ such that $A_{31}=0.5$, and in the asymmetric configuration $A_{32}=0.5$ while $A_{21}=0.05$. In each case, densities are computed to conform to these desired Atwood numbers.

Periodic boundary conditions are set in the x and y dimensions, and nonpenetrating wall boundaries are set at $z=-2\pi$ and $z=2\pi$. A hydrostatic pressure field is specified such that the mixing layer remains nominally centered around $z=0$. Constant mesh spacing is utilized in all dimensions, such that the number of grid points in the z dimension, N_z, is equal to twice the number of grid points in the x and y dimensions; in other words, $N_z=2N_y=2N_x$. For these simulations, $N_z=1152$ for a total of about 382 million computational elements.

An initial perturbation is specified at each of the two material interfaces in Fourier space as a function of maximal and minimal wave numbers $\kappa_{\rm max}$ and $\kappa_{\rm min}$ according to

$$\xi(x,y)=\sum_{j=\kappa_{\rm min}}^{\kappa_{\rm max}}\sum_{k=\kappa_{\rm min}}^{\kappa_{\rm max}}\frac{\Delta}{\kappa_{\rm max}-\kappa_{\rm min}+1}\cos\left(jx+\theta_{x,j}\right)\times\sin\left(ky+\theta_{y,k}\right), \tag{27}$$

where Δ indicates the mesh spacing and the phase shift vectors $\theta_{x,j}$ and $\theta_{y,k}$ are drawn from uniformly distributed random numbers between 0 and 2π. The mixture density at each interface at time $t=0$ is then given by

$$\rho(x,y,z)=\rho_L+\frac{\rho_H-\rho_L}{2.0}\left\{1+\tanh\left[\frac{z-\xi(x,y)}{4\Delta}\right]\right\}. \tag{28}$$

where the subscripts L and H refer, respectively, to the light and heavy densities at each interface. A broadband initial perturbation spectrum is specified such that $\kappa_{\rm min}=6$, and $\kappa_{\rm max}=96$.

Simulations are evolved in *Miranda* using an ideal gas equation-of-state (EOS) until h_{99}, the mixing width defined as the distance between 99% contours of $\widetilde{Y}_1$ and $\widetilde{Y}_3$, reaches 2π (50% of the domain size in z). During this early time, no reactions occur, and evolution is purely hydrodynamic. Once $h_{99}=2\pi$, electron and ion temperatures are set to 10 keV everywhere, and the problem is continued with radiation diffusion and TN burn physics in the *Ares* code. Additionally, at this time which shall be denoted as $t_{\rm burn}$, gravitational acceleration is turned off, boundary conditions at $z=\pm2\pi$ are changed to extrapolation, and EOSs are changed to tabular Livermore EOS (LEOS) 1018 and LEOS 5350 for the gas and plastic, respectively [52,53]. Table V summarizes material compositions for times $t\geqslant t_{\rm burn}$. DT gas is assumed to consist of a 3:1 DT mixture by atom fraction, and plastics consist of carbon and hydrogen in an atom ratio of 1.35:1. The simulation is then continued in *Ares* until the average electron temperature drops below 0.5 keV. Prior simulations [9] and experimental observations by Haines *et al.* [54] have demonstrated that the existence of spatial temperature variations can have a nonnegligible impact on the observed reaction rate. Therefore, to eliminate this potential complication in comparisons with RANS results, a preliminary LES is first run to obtain a realistic temperature time history. Then, a secondary simulation is then carried out in which spatial variation in temperature is eliminated by imposing a spatially uniform, time-varying temperature profile obtained from the preliminary simulation. While a spatially uniform temperature profile is used in the present work for the purpose of creating an idealized problem more suitable for comparison with RANS, it is worth noting that mixing layers with a photon mean free path $\lambda<<h_{99}$ should be well approximated by this idealized problem. In work by Olson *et al.* [55], for instance,

TABLE IV. Summary of problem configurations. Densities in units of mg/cm^3.

Configuration	A_{32}	A_{21}	A_{31}	ρ_3	ρ_2	ρ_1
Symmetric	0.268	0.268	0.500	10.0	5.77	3.33
Asymmetric	0.500	0.050	0.537	10.0	3.33	3.02

TABLE V. Summary of material compositions during burn phase. DT gas is 3:1 mixture, and plastics consist of carbon and hydrogen in an atom ratio of 1.35:1.

Case	Material 1	Material 2	Material 3
Premixed	CH	DT	CH
Nonpremixed	T	CH	CD

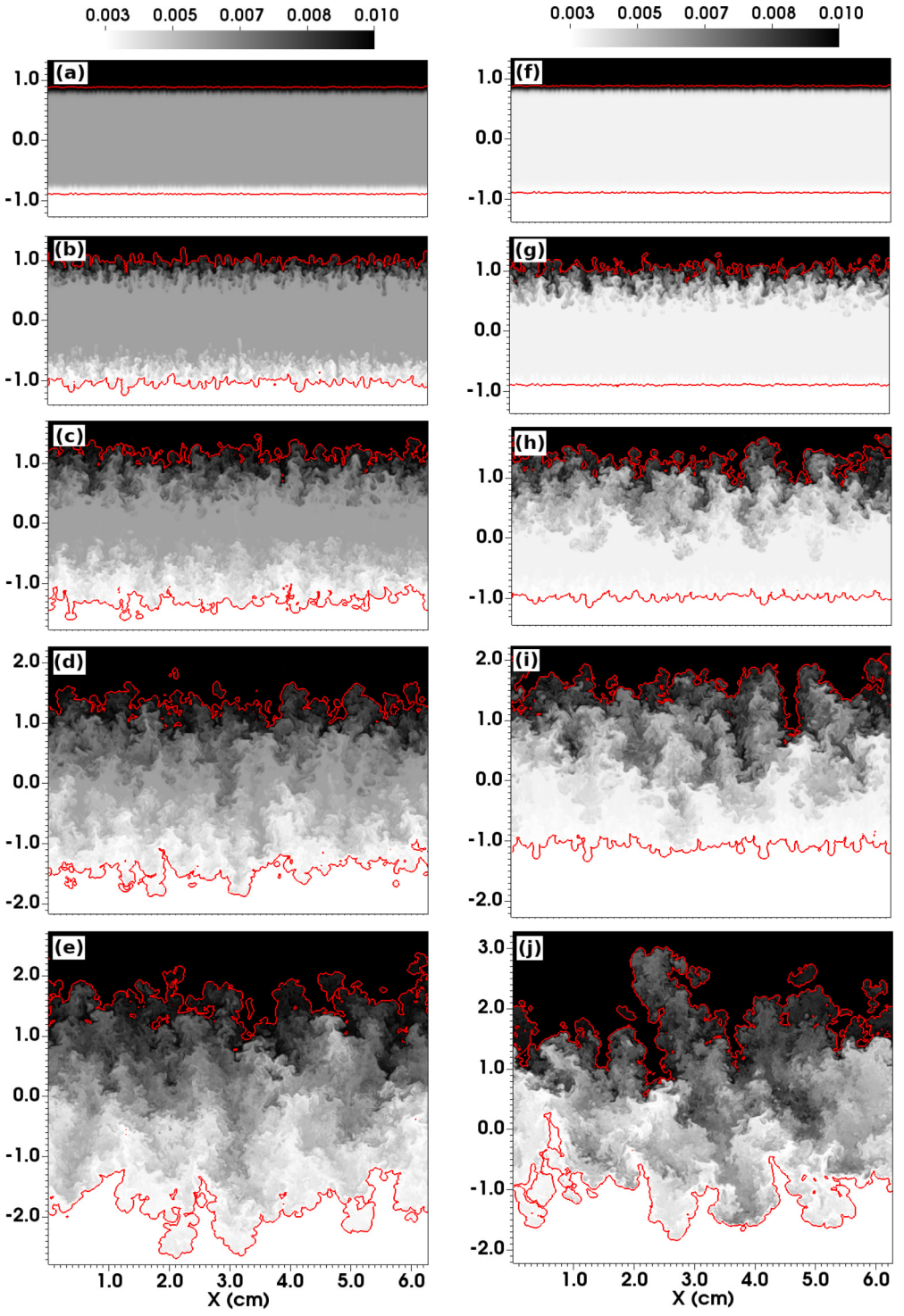

FIG. 2. Instantaneous contours of density in the $y = \pi$ plane at several time instants for the symmetric [(a)–(e)] and asymmetric [(f)–(j)] configurations. Contours of $Y_2 = 0.01$ have been overlaid in red. (a) $t/t_0 = 0.0$, (b) $t/t_0 = 5.93$, (c) $t/t_0 = 11.7$, (d) $t/t_0 = 16.6$, (e) $t/t_0 = 22.5$, (f) $t/t_0 = 0.0$, (g) $t/t_0 = 6.14$, (h) $t/t_0 = 12.3$, (i) $t/t_0 = 17.2$, and (j) $t/t_0 = 23.3$.

it was observed that ICF capsules filled with an argon-tritium gas mixture demonstrated reduced shock flash temperature compared with capsules filled with protium-tritium due to enhanced coupling with the radiation field.

In this way, large-eddy simulations are carried out in three parts. First, a hydrostatic three-component RT mixing layer is evolved using the *Miranda* code. During this stage of simulation, no reactions are occurring, and the problem is purely a hydrodynamic one. Then, once the mixing layer is well mixed, a second stage proceeds using the *Ares* code to compute the TN reactions with a fully coupled radiation-hydrodynamics treatment. During this second stage of simulation, turbulent fluctuations in temperature may exist, and an average temperature history is extracted. In the third and final stage, the

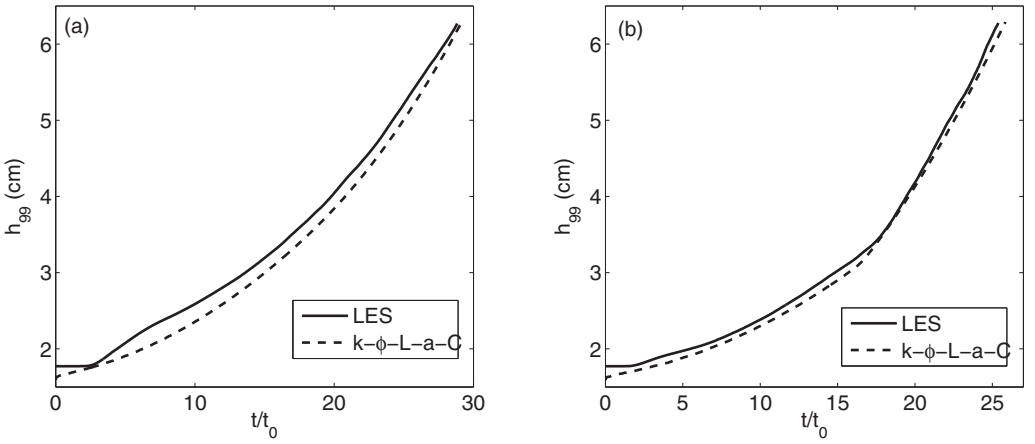

FIG. 3. Comparison of time evolution of the mixing layer width h_{99} between LES and RANS with the $k-\phi-L-a-\mathcal{C}$ model. (a) Symmetric configuration and (b) asymmetric configuration.

Ares calculation is repeated with a spatially uniform, time-varying temperature profile set to the average temperature history extracted from the previous stage. By computing turbulence statistics obtained during the reacting stages of the calculation, it is possible to obtain validation data by which to evaluate the $k-L-a-\mathcal{C}$ RANS model and the average reaction rate closure given by Eq. (25). Note that a similar three-stage procedure was used previously by Morgan *et al.* to evaluate the $k-L-a-V$ RANS model in the context of a two-component reacting mixing layer [9].

D. RANS problem setup and initial conditions

RANS simulations are conducted with the $k-\phi-L-a-\mathcal{C}$ model in *Ares*. For comparison purposes, results will also be shown with a multicomponent extension of the $k-L-a-V$ model [9,20,21], which will be referred to as the $k-L-a-\mathcal{C}$ model and utilizes the same multicomponent extension outlined by Eqs. (14), (20), and (25). These models are expected to differ primarily by the form of their spatial profiles. Simulations are performed on a 1D mesh with 576 uniformly spaced computational zones extending from $z=-2\pi$ to $z=2\pi$ with nonpenetrating walls at the boundaries. Problems are set to match the LES as closely as possible with the same material densities and compositions as described in the previous section. As in the LES problem, a constant gravitational acceleration in the negative z dimension is balanced by a hydrostatic pressure gradient such that during the nonreacting stage of the problem, the mixing layer remains nominally centered about $z=0$. Turbulence quantities are initialized such that $L_{t=0}=0.004\,\text{cm}$, $k_{t=0}=1.0\times10^{-10}$ $\text{cm}^2/\mu\text{s}^2$, and $\phi_{t=0}=\sqrt{k_{t=0}}$ in the two computational zones bordering the material interfaces at $z=\pm\frac{\pi}{4}$.

As in the LES problem, the mixing layer is allowed to evolve without reactions and with an ideal gas EOS until $h_{99}=2\pi$. After this point, electron and ion temperatures are set to 10 keV everywhere, ideal gas EOSs are changed to tabular LEOS 1018 and 5350, and the problem is continued with radiation diffusion and TN burn physics. Additionally at t_{burn}, gravitational acceleration is turned off, and the boundary conditions are set to extrapolation. Temperature in RANS simulations is specified everywhere to equal the mass-weighted average temperature time history obtained from LES.

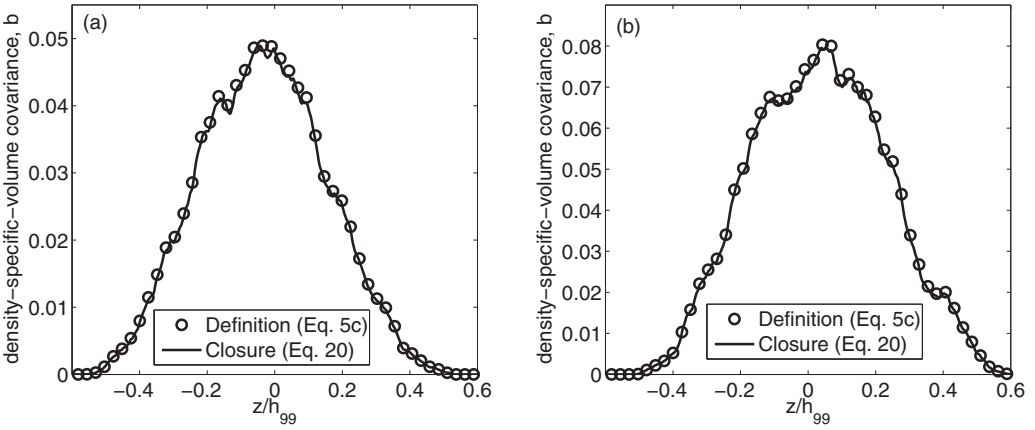

FIG. 4. *A priori* evaluation of proposed closure for b at $t=t_{\text{burn}}$. Symbols represent direct evaluation of Eq. (5c), and solid lines represent direct evaluation of Eq. (20) from LES data. (a) Symmetric configuration and (b) asymmetric configuration.

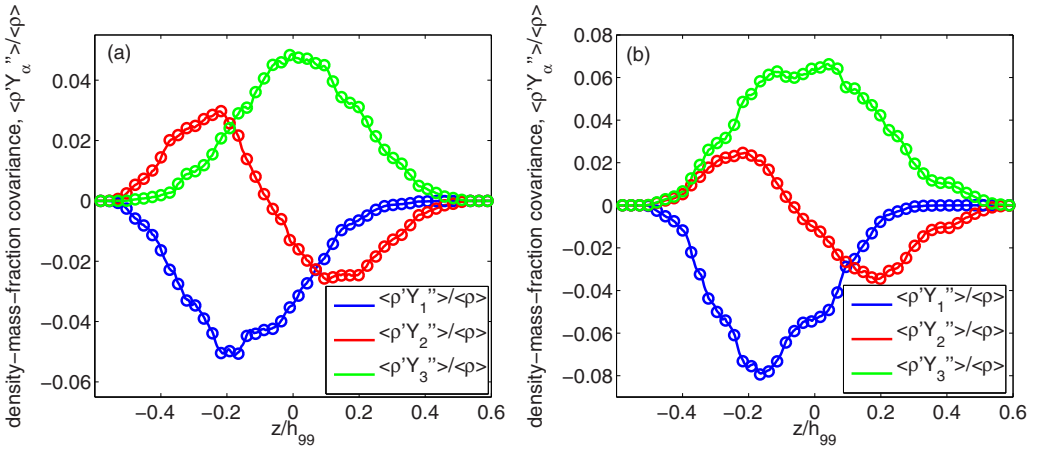

FIG. 5. *A priori* evaluation of proposed closure for $\overline{\rho' Y_\alpha''}/\overline{\rho}$ at $t = t_{\text{burn}}$. Symbols represent direct evaluation, and solid lines represent evaluation of Eq. (24) from LES data. (a) Symmetric configuration and (b) asymmetric configuration.

III. RESULTS AND DISCSSION

A. Nonreacting mixing layer

Before considering behavior of the reacting mixing layer problem, it is first desirable to examine the multicomponent mixing layer as it undergoes purely hydrodynamic evolution prior to $t = t_{\text{burn}}$. Figure 2 provides a qualitative impression of the mixing layer growth at several time instants, where the nondimensional timescale t_0 is defined according to

$$t_0 \equiv \sqrt{\frac{l_0}{A_{31} g}}, \tag{29}$$

and the reference length scale l_0 is taken as

$$l_0 \equiv \frac{4\pi}{\kappa_{\max} - \kappa_{\min}}. \tag{30}$$

In Fig. 2, instantaneous contours of density in the $y = \pi$ plane are plotted at several time instants for both the symmetric and asymmetric configurations. These contours illustrate how both interfaces quickly become unstable due to the multimode initial perturbation and how eventually heavy spikes of material 3 eventually penetrate all the way into material 1, leading to a highly turbulent, well-mixed layer at late time. In the symmetric configuration, illustrated in Figs. 2(a) through 2(e), both interfaces grow at roughly the same rate; whereas in the asymmetric configuration illustrated in Figs. 2(f) through 2(j), the upper interface with higher Atwood number develops much more rapidly than the lower interface. This asymmetric mixing behavior is particularly noticeable by considering the red contour of $Y_2 = 0.01$ in Figs. 2(g) and 2(h). In these images, the upper contour is clearly observed to contain more structure and greater amplitude perturbations than the lower contour. Of course, this behavior is expected by the widely used model for RT growth that says in the limit of self-similarity, the mixing layer width should grow approximately according to

$$h(t) \approx \alpha A g t^2. \tag{31}$$

In Eq. (31), α is a constant growth parameter, and A is the interfacial Atwood number.

Figure 3 plots the time evolution of the mixing layer width h_{99} for both LES results and RANS results using the $k - \phi - L - a - \mathcal{C}$ model. For the present work, RANS results are generated with model coefficients constrained to reproduce a

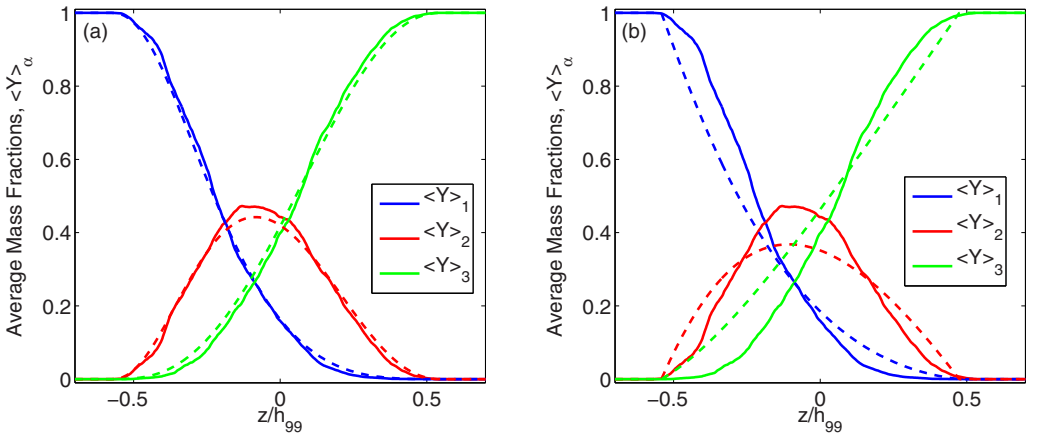

FIG. 6. Comparison between LES and RANS of average mass fraction profiles $\widetilde{Y}_\alpha$ in the symmetric configuration at $t = t_{\text{burn}}$. (a) LES (solid lines) versus the $k - \phi - L - a - \mathcal{C}$ model (dashed lines). (b) LES (solid lines) versus the $k - L - a - \mathcal{C}$ model (dashed lines).

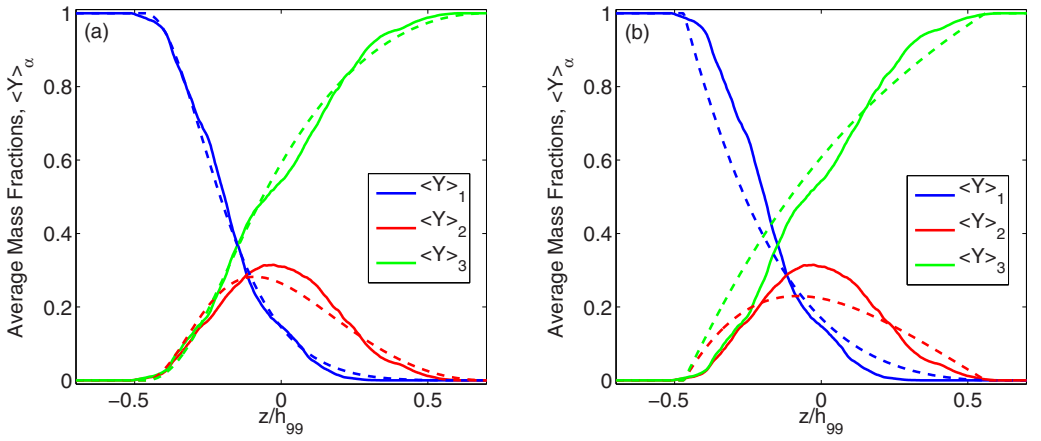

FIG. 7. Comparison between LES and RANS of average mass fraction profiles $\widetilde{Y}_\alpha$ in the asymmetric configuration at $t = t_{\text{burn}}$. (a) LES (solid lines) versus the $k-\phi-L-a-\mathcal{C}$ model (dashed lines). (b) LES (solid lines) versus the $k-L-a-\mathcal{C}$ model (dashed lines).

self-similar RT growth rate of $\alpha = 0.03$. As seen in Fig. 3, this choice agrees reasonably well with LES for both the symmetric and asymmetric configurations. Where the RANS results demonstrate quadratic growth virtually from time $t/t_0 = 0$, however, the LES results require some amount of time to transition to turbulence before quadratic growth is achieved. By design, the present LES is run with a broadband initial perturbation spectrum and with zero molecular viscosity; both choices are intended to minimize the time required for the LES reach a self-similar state. As Fig. 3 shows, both the LES and RANS grow at a similar rate for times $t/t_0 \gtrsim 12$ and can therefore both be expected to be in a comparable self-similar state at $t = t_{\text{burn}}$ when h_{99} reaches 2π. Interestingly, both LES and RANS indicate an inflection in h_{99} in the asymmetric case occurring around $t/t_0 \approx 18$, which corresponds roughly when the heavy component penetrates into the light material and begins driving the growth of h_{99} at the lower interface at a faster rate than before. This inflection is not present in the symmetric case.

Following the approach of Olson and Greenough [28], it is possible to obtain an approximation of the effective viscosity in the present LES results according to

$$\mu_{\text{eff}} = C_\mu \rho \left|\nabla^2 \mathbf{S}\right| \Delta^4, \tag{32}$$

where $\mathbf{S} \equiv (S_{ij}S_{ij})^{1/2}$ in terms of the strain-rate tensor S_{ij}, and C_μ is a code-specific constant determined previously for *Miranda* to be approximately equal to 8.11 [28,30]. Utilizing Eq. (32), an effective Taylor Reynolds number $\text{Re}_\lambda \approx 230$, and an effective large-scale Reynolds number $\text{Re} \equiv \frac{\rho h_{99} \dot{h}_{99}}{\mu_{\text{eff}}} \approx 5800$ are computed for the symmetric configuration at the end of the nonreacting phase ($t = t_{\text{burn}}$). Based on this approximation for Re_λ, the mixing layer is expected to be fully developed according to the Dimotakis criterion [56].

Before delving into additional comparisons between LES and RANS, however, it is first desirable to utilize the LES results to evaluate proposed RANS closures given by Eqs. (20) and (24) in an *a priori* fashion. Figure 4 evaluates the closure for b in both the symmetric and asymmetric configurations. In this figure, symbols represent direct evaluation of the definition of b given by Eq. (5c), while solid lines represent evaluation of the closure given by Eq. (20), which is computed from mass fraction covariances like the RANS model

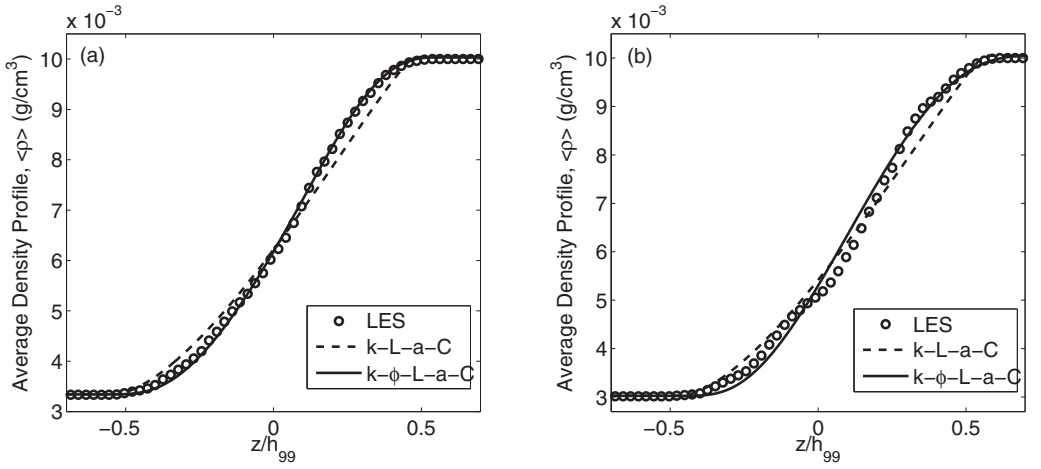

FIG. 8. Comparison of average density profiles $\overline{\rho}$ at $t = t_{\text{burn}}$. (a) Symmetric configuration and (b) asymmetric configuration.

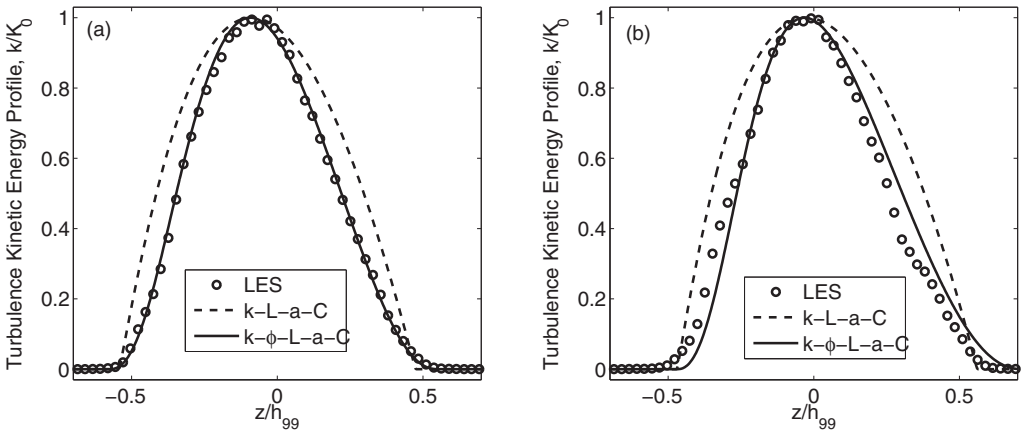

FIG. 9. Comparison of normalized turbulence kinetic energy profiles k/K_0 at $t = t_{\text{burn}}$. (a) Symmetric configuration and (b) asymmetric configuration.

would do. In both the symmetric and asymmetric cases, the two expressions for b are found to be in close agreement, which provides confidence that Eq. (20) is an accurate closure for the density-mass-fraction-covariance, which is important to accurate prediction of buoyancy production in the RANS model.

Similarly, Fig. 5 evaluates the proposed closure for the density-mass-fraction covariance, $\overline{\rho' Y_\alpha''}$, in both the symmetric and asymmetric configurations. In Fig. 5, symbols represent direct evaluation of $\overline{\rho' Y_\alpha''}$ from LES, while solid lines represent evaluation of the closure proposed by Eq. (24). As with the closure for b, Eq. (24) utilizes mass fraction covariances to close $\overline{\rho' Y_\alpha''}$ terms, as the RANS model would do. In both the symmetric and asymmetric cases, the closure is found to be in close agreement with direct evaluation, which provides confidence in Eq. (24). While the density-mass-fraction covariance does not appear in the RANS equations for purely hydrodynamic evolution, it does appear in the reaction rate closure given by Eqs. (23) and (25) and therefore will be important in Sec. III B when considering the case of the reacting mixing layer.

Figures 6 and 7 illustrate the extent of multicomponent mixing that is occurring by plotting average mass fractions $\widetilde{Y}_\alpha$ at time $t = t_{\text{burn}}$ in the symmetric and asymmetric configurations, respectively. In addition, these figures compare the average profiles obtained with LES with those predicted by the $k - \phi - L - a - \mathcal{C}$ and $k - L - a - \mathcal{C}$ RANS models. By definition, t_{burn} is the time at which $h_{99} = 2\pi$; so, it is not surprising that the LES and RANS results generally agree on the width of the mixing profiles at this time. What is interesting, however, is the level of agreement in the shape of the profiles and in particular the magnitude of the peak value of $\widetilde{Y}_2$. Although the $k - L - a - \mathcal{C}$ model is able to generally capture some of the qualitative behavior, results with this model are clearly limited by assumption of a linear mixing profile. As a result, there is significant discrepancy between LES and $k - L - a - \mathcal{C}$, particularly in the tails. With the $k - \phi - L - a - \mathcal{C}$ model, which is designed to achieve higher-order spatial profiles, a much higher level of agreement is achieved between LES and RANS in both the shape of profiles and in the peak magnitude of $\widetilde{Y}_2$.

Figures 8–10 further compare LES and RANS results at $t = t_{\text{burn}}$ by plotting, respectively, profiles of average density, turbulence kinetic energy, and density-specific-volume covariance. In Fig. 8, average density profiles are found to be in reasonable agreement between LES and the two RANS

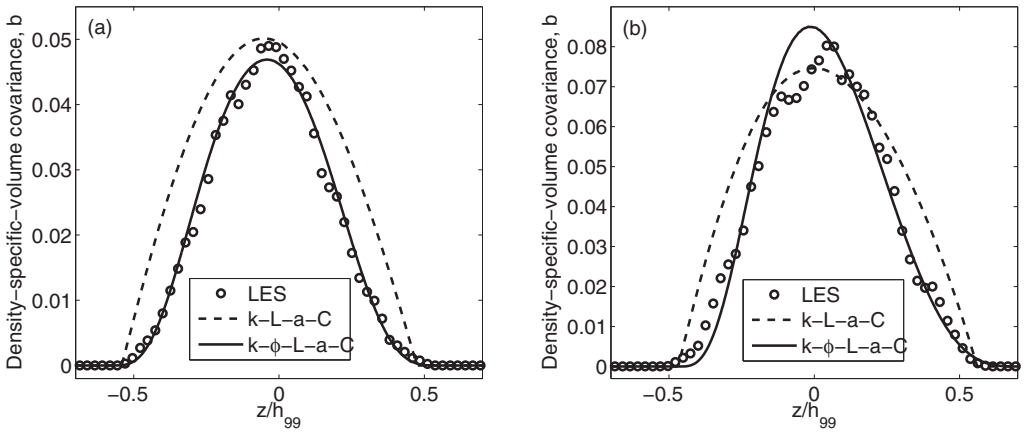

FIG. 10. Comparison of density-specific-volume covariance b at $t = t_{\text{burn}}$. (a) Symmetric configuration and (b) asymmetric configuration.

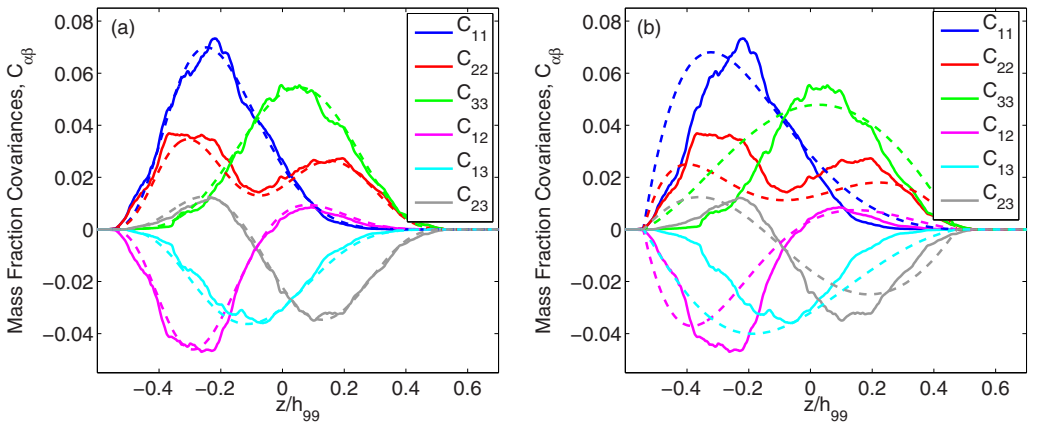

FIG. 11. Comparison between LES and RANS of mass fraction covariance profiles $\mathcal{C}_{\alpha\beta}$ in the symmetric configuration at $t = t_{\text{burn}}$. (a) LES (solid lines) versus the $k-\phi-L-a-\mathcal{C}$ model (dashed lines). (b) LES (solid lines) versus the $k-L-a-\mathcal{C}$ model (dashed lines).

models; although, the $k-\phi-L-a-\mathcal{C}$ model is again observed to agree more closely with LES than $k-L-a-\mathcal{C}$ due to the high-order nature of the profiles achieved by the $k-\phi-L-a-\mathcal{C}$ model. In Fig. 9, profiles of k across the mixing layer are normalized by K_0, the peak value of k, for purposes of comparing profile shape between LES and RANS. Recall that since the RANS models do not capture the transition to turbulence, it is not expected that the magnitude K_0 should necessarily agree between LES and RANS for a given instant in time. As illustrated in Fig. 9, however, the high-order profile achieved by the $k-\phi-L-a-\mathcal{C}$ model is again in closer agreement with LES than the quadratic profile predicted by the $k-L-a-\mathcal{C}$ model. Similarly, profiles of b are observed to be in reasonably close agreement between LES and RANS in Fig. 10. Where earlier results in Fig. 4 showed the closure for b given by Eq. (20) to be accurate in an *a priori* comparison, results in Fig. 10 additionally show this to be the case when for comparisons made in an *a posteriori* fashion. As with other results, the $k-\phi-L-a-\mathcal{C}$ model agrees more closely with LES in the shape of the b profile than the $k-L-a-\mathcal{C}$ model.

Finally, in Figs. 11 and 12, profiles of mass fraction covariances are compared between LES and RANS for the symmetric and asymmetric configurations. In these figures, LES results are obtained through direct evaluation of second moment statistics, RANS results for off-diagonal covariances ($\mathcal{C}_{12}$, $\mathcal{C}_{13}$, and $\mathcal{C}_{23}$) are transported according to Eq. (14), and RANS results for diagonal elements ($\mathcal{C}_{11}$, $\mathcal{C}_{22}$, and $\mathcal{C}_{33}$) are constructed from the off-diagonal elements according to Eq. (21). While both the $k-\phi-L-a-\mathcal{C}$ and $k-L-a-\mathcal{C}$ models generally capture the qualitative behavior of the LES results, the $k-\phi-L-a-\mathcal{C}$ model results demonstrate a remarkable level of agreement in both the shape and magnitude of all six covariance components, particularly in the symmetric configuration. This level of agreement demonstrates that the $k-\phi-L-a-\mathcal{C}$ is able to accurately capture the characteristics of the three-component mixing problem most important to reaction rate modeling.

B. Reacting mixing layer

Results of the reacting mixing layer are considered next. Recall, once $t = t_{\text{burn}}$ (i.e., when h_{99} reaches 2π), electron and ion temperatures are set to 10 keV everywhere, and the problem is continued with TN burn physics. A preliminary LES is first run to obtain a realistic temperature time history, and the mass-weighted average temperatures from this preliminary

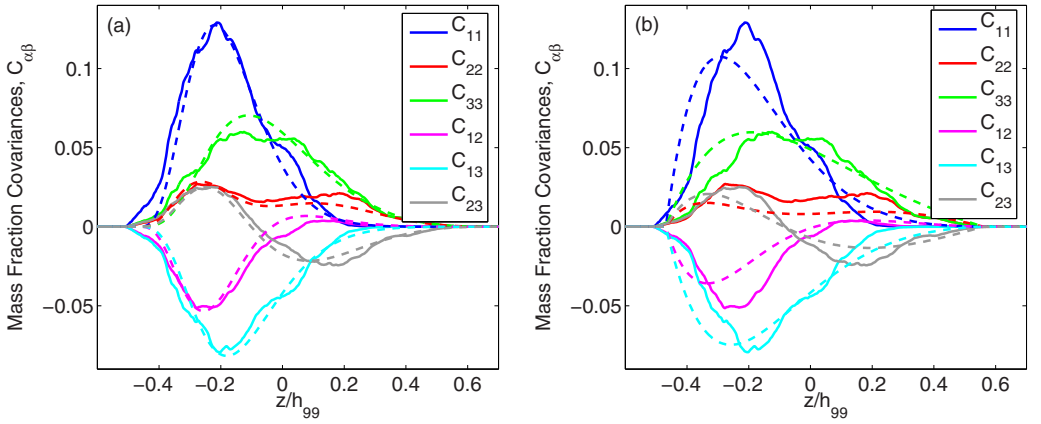

FIG. 12. Comparison between LES and RANS of mass fraction covariance profiles $\mathcal{C}_{\alpha\beta}$ in the asymmetric configuration at $t = t_{\text{burn}}$. (a) LES (solid lines) versus the $k-\phi-L-a-\mathcal{C}$ model (dashed lines). (b) LES (solid lines) versus the $k-L-a-\mathcal{C}$ model (dashed lines).

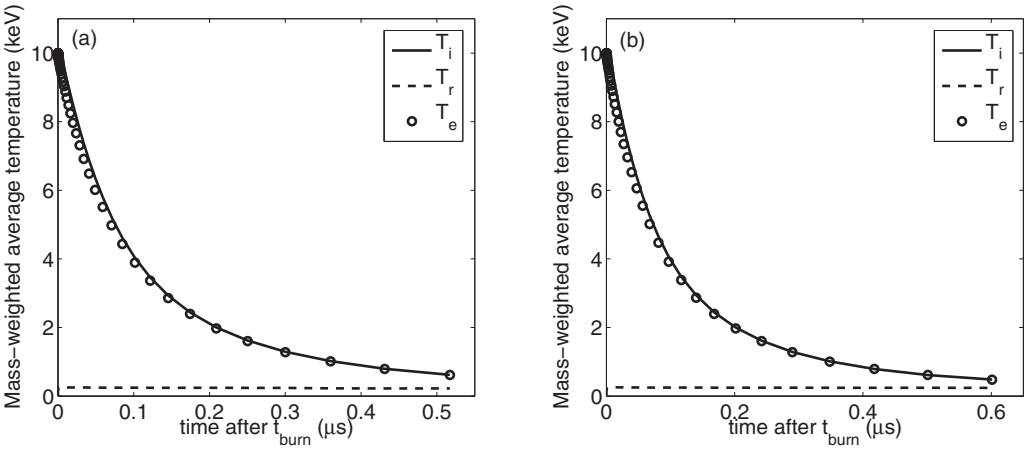

FIG. 13. Mass-weighted average ion (T_i), electron (T_e), and radiation (T_r) temperature history of burning mixing layer with premixed reactants from LES in (a) symmetric and (b) asymmetric configurations.

simulation are then imposed everywhere in follow-on LES and RANS simulations. Figure 13 plots the temperature time history that is used for the premixed case in both the symmetric and asymmetric configurations. Little separation occurs between the ion and electron temperatures, and the radiation temperature reaches a nearly steady value that peaks around 0.25 keV and decays to around 0.22 keV. The temperature histories plotted in this figure are obtained from preliminary LES calculation; they are then imposed uniformly in both follow-on LES and RANS calculations. This allows for direct evaluation of the reaction rate closure given by Eq. (25) under the condition that fluctuations in temperature (and therefore also in reaction cross section) can be neglected.

Figure 14 plots the total TN neutrons produced as a function of time for simulations with premixed reactants in both the symmetric and asymmetric configurations. LES results are compared against two sets of $k-\phi-L-a-\mathcal{C}$ RANS results. Dashed lines in Fig. 14 indicate RANS results that include no modification to reaction rate due to turbulent fluctuations (i.e., taking $C_{\alpha\beta}=0$), and solid lines indicate RANS results that utilize Eq. (25) to close the average reaction rate. RANS results that utilize Eq. (25) are found to be in remarkably close agreement with LES, while those results that include no modification to reaction rate (which essentially assumes mixing is purely atomic) underpredicts total TN neutrons by approximately 20% for the symmetric case and by 30% for the asymmetric case.

Figure 15 shows the temperature time history obtained for simulations with nonpremixed reactants in the symmetric and asymmetric configurations. As with the premixed case, the time histories presented in this figure were obtained as averaged temperatures from a preliminary LES calculation and then imposed as a spatially uniform temperature history in follow on LES and RANS calculations. Similarly to the premixed case, ion and electron temperatures show little separation, and the radiation temperature decays slowly from about 0.26 keV to about 0.17 keV at the end of the simulation.

Figure 16 then plots the total TN neutrons produced as a function of time for simulations with nonpremixed reactants in the symmetric and asymmetric configurations. Again, LES

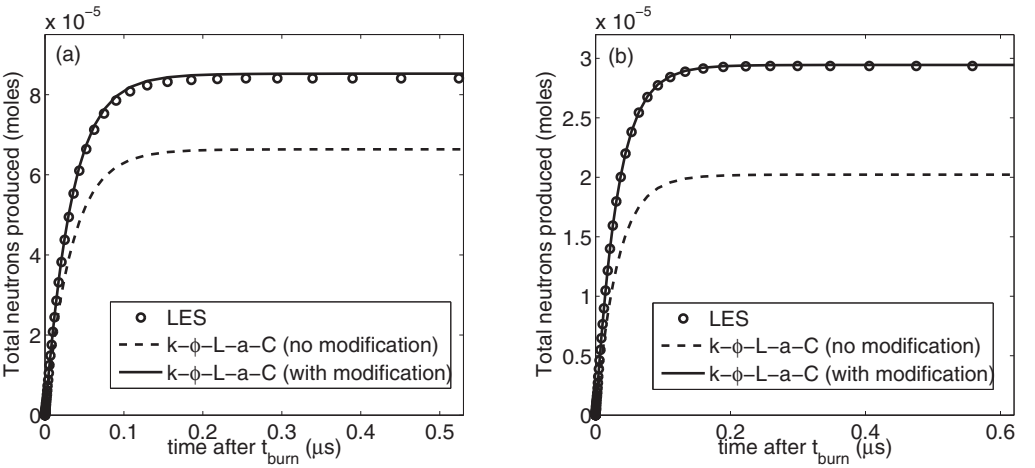

FIG. 14. Comparison of total neutron production as a function of time for LES and RANS with the $k-\phi-L-a-\mathcal{C}$ model for mixing layer with premixed reactants. RANS results shown with and without modification to the reaction rate described by Eq. (25). (a) Symmetric configuration and (b) asymmetric configuration.

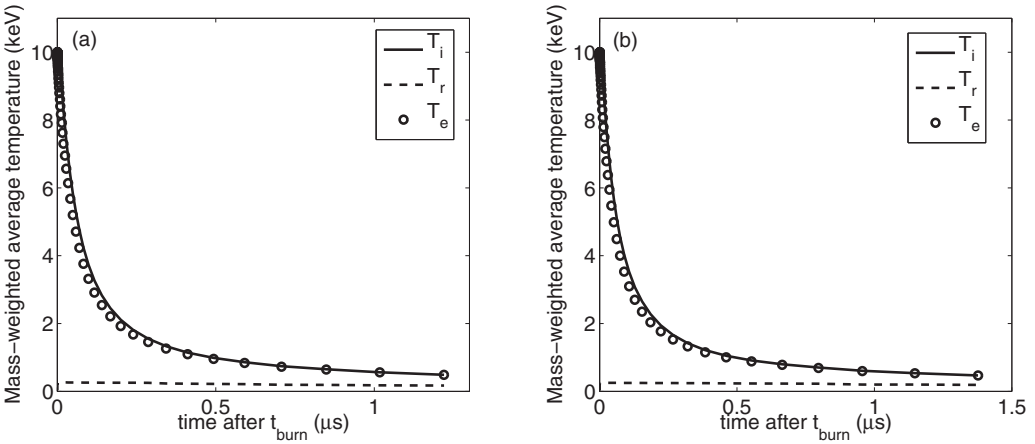

FIG. 15. Mass-weighted average ion (T_i), electron (T_e), and radiation (T_r) temperature history of burning mixing layer with nonpremixed reactants from LES in (a) symmetric and (b) asymmetric configurations.

results are compared against two sets of RANS results—one set in which no modification is made to the average reaction rate, and a second in which Eq. (25) is used to model the impact of turbulence on the average reaction rate. While the agreement between LES and RANS in this case is not as close as in the premixed case, utilizing Eq. (25) is observed to reduce overprediction of total neutrons from 115% to 30% in the symmetric configuration and from 106% to 17% in the asymmetric configuration. In contrast to the premixed case in which reactions can occur anywhere with component 2, in the nonpremixed case, reactions can only occur in areas where component 1 mixes diffusively with component 3. Generally speaking, this means that the nonpremixed case tends to be more sensitive to effects of numerical diffusion, which might account for some of the remaining discrepancy between LES and RANS results. Overall though, the results of Figs. 14 and 16 suggest that the $k-\phi-L-a-\mathcal{C}$ RANS model with appropriate modification to the average reaction rate is able to reasonably predict key metrics of TN burn when temperature fluctuations can be neglected.

IV. SUMMARY AND CONCLUSIONS

In the present work, the impact of contaminants in problems of reacting turbulent mixing has been examined in the context of a three-component RT mixing problem. First, LES of a nonreacting RT mixing layer with three components was performed to obtain a high-fidelity baseline against which to compare lower-fidelity RANS calculations. This LES was performed in symmetric and asymmetric configurations, and the nonreacting mixing layer was allowed to develop into a turbulent, well-mixed state with interpenetration of the heavy component all the way through to the light component.

In addition, a multicomponent extension to the $k-\phi-L-a-V$ model [12], termed the $k-\phi-L-a-\mathcal{C}$ model, was proposed, including treatment for the impact of turbulence on the average reaction rate. This model relaxes the assumption of only two mixing components utilized by previous models [9,12,22] and therefore is expected to better account for the presence of nonreacting contaminant components. Utilizing the high-fidelity LES, new closure models for the density-specific-volume covariance [Eq. (20)] and the

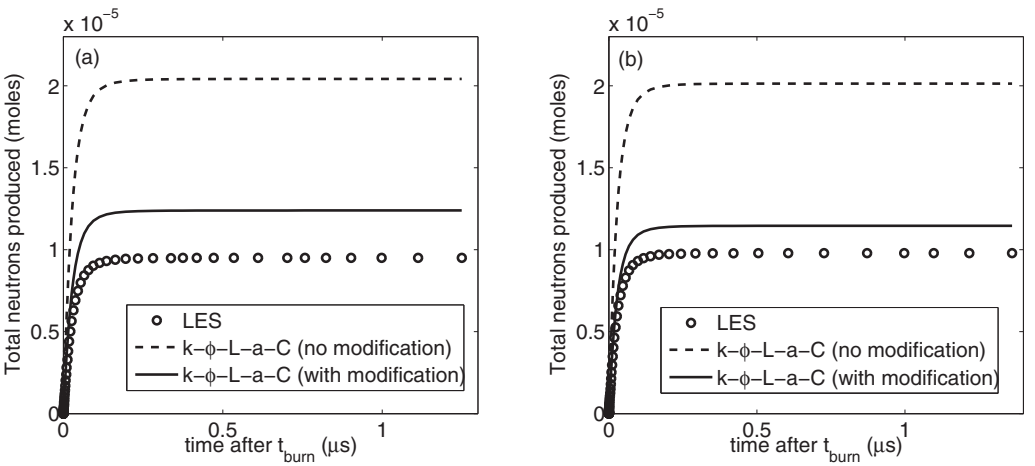

FIG. 16. Comparison of total neutron production as a function of time for LES and RANS with the $k-\phi-L-a-\mathcal{C}$ model for mixing layer with nonpremixed reactants. RANS results shown with and without modification to the reaction rate described by Eq. (25). (a) Symmetric configuration and (b) asymmetric configuration.

density-mass-fraction covariances [Eq. (24)] were evaluated in an *a priori* fashion and demonstrated to provide accurate closure.

Comparisons for the nonreacting mixing layer at time $t = t_{\text{burn}}$ showed a high level of agreement between LES and RANS results with the $k-\phi-L-a-\mathcal{C}$ model in profiles of average mass fraction, average density, turbulence kinetic energy, density-specific-volume covariance, and in the shape and magnitude of the six components of the covariance matrix. RANS results with the simpler $k-L-a-\mathcal{C}$ model demonstrated an ability to capture the qualitative behavior of the LES but exhibited a greater degree of discrepancy in both magnitude and shape of the spatial profiles considered. Differences between the $k-\phi-L-a-\mathcal{C}$ model and the $k-L-a-\mathcal{C}$ model highlight the benefit of the high-order spatial profiles admitted by the $k-\phi-L-a-\mathcal{C}$ model which allow it to achieve a high degree of agreement with LES.

Next, LES and RANS calculations were performed of the three-component RT mixing layer as it underwent TN burn. To create a grounds for common comparison, a spatially uniform temperature history was imposed, based on results from a preliminary LES calculation. Under this constraint, the impact of spatial variations in reactant concentrations was separated from spatial variations in temperature, allowing for direct evaluation of a new proposed closure for the average reaction rate [Eq. (25)]. For premixed TN reactions occurring in the intermediate component, application of this closure resulted in a RANS prediction of total TN neutrons that agreed with LES to within 1%. RANS simulations which did not include this closure were found to underpredict TN neutron production with respect to LES by 20–30%. For the nonpremixed case, in which the intermediate material represented a contaminant between reacting light and heavy components, RANS results using Eq. (25) were found to agree with LES to within 30%, whereas results that did not include this closure overpredicted TN neutron production by over 100%. While the present work has focused on the simplistic problem of a reacting three-component mixing layer, this configuration has been chosen because it represents a simplification of the basic mixing physics found in actual ICF capsules such as the recessed-layer CD Symcap experiments [13,14]. These results suggest that significant errors in RANS-based ICF simulations may arise if the impact of turbulence on reaction rate is neglected or is modeled inaccurately.

Overall, this work has shown that the new $k-\phi-L-a-\mathcal{C}$ model is able to provide a high level of agreement with LES for the reacting three-component RT mixing problem when the impact of turbulent fluctuations in the reaction cross section can be neglected. Of course, this simplification will not always be appropriate, and a more complete model should account for turbulent moments involving the fluctuating cross section. It is therefore recommended that future research focus on developing means to provide closure for these terms perhaps through modeling turbulent variations in temperature. In addition, the three-component RT problem considered in the present work represents a simplistic generalization of the basic physics of a reacting turbulent mixing layer involving contaminants. Future work should additionally seek to assess the $k-\phi-L-a-\mathcal{C}$ model in application to more realistic ICF problems. Based on the present work, it is expected that the $k-\phi-L-a-\mathcal{C}$ model, with its high-order spatial profiles and multicomponent treatment for turbulent variations in reactant concentrations, should agree more closely with experiment than earlier simulations with the $k-L-a-V$ model [14].

ACKNOWLEDGMENTS

The author thanks M. Ulitsky, P. Rambo, B. Olson, O. Schilling, B. Pudliner, and other colleagues at LLNL for their helpful input and discussions in preparation of this work. This work was performed under the auspices of the U.S. Department of Energy by Lawrence Livermore National Laboratory under Contract No. DE-AC52-07NA27344.

APPENDIX: GOVERNING EQUATIONS

1. Hydrodynamics equations

The governing equations are the compressible Navier-Stokes equations for a multicomponent, reacting flow:

$$\frac{\partial \rho}{\partial t}+\frac{\partial(\rho u_i)}{\partial x_i}=0, \tag{A1}$$

$$\frac{\partial(\rho Y_\alpha)}{\partial t}+\frac{\partial(\rho Y_\alpha u_i)}{\partial x_i}=-\frac{\partial J_{\alpha,i}}{\partial x_i}+\dot{r}_\alpha, \tag{A2}$$

$$\frac{\partial(\rho u_j)}{\partial t}+\frac{\partial(\rho u_i u_j)}{\partial x_i}=-\frac{\partial p}{\partial x_j}+\frac{\partial \tau_{ij}}{\partial x_i}+\rho g_j, \tag{A3}$$

$$\frac{\partial E}{\partial t}+\frac{\partial[(E+p)u_i]}{\partial x_i}=\frac{\partial(\tau_{ij}u_i)}{\partial x_j}-\frac{\partial q_i}{\partial x_i}+\rho g_i u_i+\dot{Q}. \tag{A4}$$

In Eqs. (A1) through (A4), ρ is density, t is time, u_i is the velocity vector, x_i is the spatial coordinate vector, Y_α is the mass fraction of species α, $J_{\alpha,i}$ is the diffusive mass flux of species α, $\dot{r}_\alpha$ is the reaction rate of species α, p is pressure, τ_{ij} is the viscous stress tensor, g_j is a gravitational body force vector, E is the total energy, q_i is the heat flux vector, and $\dot{Q}$ is the heat source term. The diffusive mass flux is given in terms of effective binary diffusion coefficients D_α as

$$J_{\alpha,i}=-\rho\left(D_\alpha\frac{\partial Y_\alpha}{\partial x_i}-Y_\alpha\sum_{\beta=1}^{N}D_\beta\frac{\partial Y_\beta}{\partial x_i}\right), \tag{A5}$$

for k=1, 2, ..., N total species. The viscous stress tensor is given by

$$\tau_{ij}=2\mu S_{ij}+\left(\beta-\frac{2}{3}\mu\right)\frac{\partial u_i}{\partial x_i}\delta_{ij}, \tag{A6}$$

where μ is the shear viscosity, β is the bulk viscosity, δ_{ij} is the Kronecker delta, and S_{ij} is the strain rate tensor,

$$S_{ij}=\frac{1}{2}\left(\frac{\partial u_i}{\partial x_j}+\frac{\partial u_j}{\partial x_i}\right). \tag{A7}$$

The heat flux vector is given in terms of the thermal conductivity κ, the temperature T, and species enthalpy h_α,

$$q_i=-\kappa\frac{\partial T}{\partial x_i}+\sum_{\alpha=1}^{N}h_\alpha J_{\alpha,i}. \tag{A8}$$

Component temperature, enthalpy, and pressure are obtained through the EOS as a function of component partial density and specific internal energy. These relationships are given functionally as

$$p_\alpha = P_{\rm EOS}(e_\alpha, \rho_\alpha), \tag{A9a}$$

$$T_\alpha = T_{\rm EOS}(e_\alpha, \rho_\alpha), \tag{A9b}$$

$$h_\alpha = H_{\rm EOS}(e_\alpha, \rho_\alpha). \tag{A9c}$$

Using an assumption of pressure and temperature equilibrium, an iterative process is used to solve for component volume fractions, v_α, which allows the determination of partial densities and energies according to

$$\rho_\alpha = \frac{Y_\alpha \rho}{v_\alpha}, \tag{A10}$$

and

$$e = \frac{E}{\rho} - \frac{1}{2}u_i u_i = \sum_{\alpha=1}^{N} Y_\alpha e_\alpha \ . \tag{A11}$$

Total pressure is then determined according to the mixture relationship

$$p = \sum_{\alpha=1}^{N} v_\alpha p_\alpha. \tag{A12}$$

2. Radiation diffusion equations

In the present work, coupling between radiation and hydrodynamics is treated with a Planckian nonequilibrium diffusion model. A single opacity, ω, is used to characterize both the energy absorbed from the radiation field and the energy contributed from the material to the radiation field via emission. The radiation energy E_r is then evolved according to

$$\frac{\partial E_r}{\partial t} = \frac{\partial}{\partial x_i}\left(\frac{c}{3\omega\rho}\frac{\partial E_r}{\partial x_i}\right) + c\omega\rho\left(a_r T_e^4 - E_r\right), \tag{A13}$$

where c is the speed of light in a vacuum, T_e is the electron temperature, and a_r is the radiation constant which is given in terms of the Stefan-Boltzmann constant $\sigma_{\rm SB}$ by

$$a_r \equiv \frac{4}{c}\sigma_{\rm SB}. \tag{A14}$$

Electron and ion energies are allowed to evolve separately, with the ion energy given by Eq. (A4) and the electron energy E_e given by,

$$\frac{\partial E_e}{\partial t} + \frac{\partial (E_e u_i)}{\partial x_i} = -\frac{\partial q_{e,i}}{\partial x_i} + \dot{Q}_e. \tag{A15}$$

The electron heat flux vector $q_{e,i}$ is given in terms of the electron conductivity κ_e by

$$q_{e,i} = -\kappa_e \frac{\partial T_e}{\partial x_i}. \tag{A16}$$

The ion and electron fields are then coupled to the radiation field through the source terms which are given by

$$\dot{Q}_e = \frac{\rho c_v K_{ie}}{\Delta_t}(T_i - T_e) + c\omega\rho\left(E_r - a_r T_e^4\right) + \dot{Q}_{{\rm TN},e}, \tag{A17}$$

$$\dot{Q} = \frac{\rho c_v K_{ie}}{\Delta_t}(T_e - T_i) + \dot{Q}_{{\rm TN},i}. \tag{A18}$$

In Eqs. (A17) and (A18), K_{ie} is the ion-electron coupling coefficient, and T_i is the ion temperature. The specific heat, electron, and ion temperatures are determined from the EOS, and the radiation temperature is related to the radiation energy by

$$E_r = a_r T_r^4. \tag{A19}$$

$\dot{Q}_{{\rm TN},e}$ and $\dot{Q}_{{\rm TN},i}$ in Eqs. (A17) and (A18) are source terms due to local deposition of energy from TN reactions.

[1] F. K. Browand and C. D. Winant, Laboratory observations of shear-layer instability in a stratified fluid, Boundary-Layer Meteorol **5**, 67 (1973).

[2] I. P. D. De Silva, H. J. S. Fernando, F. Eaton, and D. Hebert, Evolution of Kelvin-Helmholtz billows in nature and laboratory, Earth Planet. Sci. Lett. **143**, 217 (1996).

[3] J. Werne and D. C. Fritts, Stratified shear turbulence: Evolution and statistics, Geophys. Res. Lett. **26**, 439 (1999).

[4] M. C. Kelley, C. Y. Chen, R. R. Beland, R. Woodman, J. L. Chau, and J. Werne, Persistence of a Kelvin-Helmholtz instability complex in the upper troposphere, J. Geophys. Res. **110**, D14106 (2005).

[5] D. Arnett, The role of mixing in astrophysics, Astrophys. J. Suppl. S **127**, 213 (2000).

[6] J. D. Lindl, R. L. McCrory, and E. M. Campbell, Progress toward ignition and burn propagation in inertial confinement fusion, Phys. Today **45**, 32 (1992).

[7] J. Lindl, Development of the indirect-drive approach to inertial confinement fusion and the target physcis basis for ignition and gain, Phys. Plasmas **2**, 3933 (1995).

[8] T. Poinsot and D. Veynante, *Theoretical and Numerical Combustion*, 2nd ed.(R. T. Edwards, Inc., Philadelphia, PA, 2005).

[9] B. E. Morgan, B. J. Olson, W. J. Black, and J. A. McFarland, Large-eddy simulation and Reynolds-averaged Navier-Stokes modeling of a reacting Rayleigh-Taylor mixing layer in a spherical geometry, Phys. Rev. E **98**, 033111 (2018).

[10] Lord Rayleigh, Investigation of the character of the equilibrium of an incompressible heavy fluid of variable density, Proc. R. Math. Soc. **s1-14**, 170 (1882).

[11] G. I. Taylor, The instability of liquid surfaces when accelerated in a direction perpendicular to their plane, Proc. R. Soc. Lond. A **201**, 192 (1950).

[12] B. E. Morgan, Self-consistent, high-order spatial profiles in a model for two-fluid turbulent mixing, Phys. Rev. E **104**, 015107 (2021).

[13] D. T. Casey, V. A. Smalyuk, R. E. Tipton, J. E. Pino, G. P. Grim, B. A. Remington, D. P. Rowley, S. V. Weber, M. Barrios, L. R. Benedetti, D. L. Bleuel, E. J. Bond, D. K. Bradley, J. A. Caggiano, D. A. Callahan, C. J. Cerjan, K. C. Chen, D. H.

Edgell, M. J. Edwards, D. Fittinghoff *et al.*, Development of the CD Symcap platform to study gas-shell mix in implosions at the National Ignition Facility, Phys. Plasmas **21**, 092705 (2014).

[14] K. K. Mackay and J. E. Pino, Modeling gas-shell mixing in ICF with separated reactants, Phys. Plasmas **27**, 092704 (2020).

[15] M. Chertkov, V. Lebedev, and N. Vladimirova, Reactive Rayleigh-Taylor turbulence, J. Fluid Mech. **633**, 1 (2009).

[16] N. Attal and P. Ramaprabhu, The stability of reacting single-mode Rayleigh-Taylor flames, Physica D **404**, 132353 (2020).

[17] G. Dimonte and R. Tipton, K-L turublence model for the self-similar growth of the Rayleigh-Taylor and Richtmyer-Meshkov instabilities, Phys. Fluids **18**, 085101 (2006).

[18] B. E. Morgan and M. E. Wickett, Three-equation model for the self-similar growth of Rayleigh-Taylor and Richtmyer-Meshkov instabilities, Phys. Rev. E **91**, 043002 (2015).

[19] B. E. Morgan, O. Schilling, and T. A. Hartland, Two-length-scale turbulence model for self-similar buoyancy-, shock-, and shear-driven mixing, Phys. Rev. E **97**, 013104 (2018).

[20] A. Campos and B. E. Morgan, Direct numerical simulation and Reynolds-averaged Navier-Stokes modeling of the sudden viscous dissipation for multicomponent turbulence, Phys. Rev. E **99**, 063103 (2019).

[21] B. E. Morgan, Scalar mixing in a Kelvin-Helmholtz shear layer and implications for Reynolds-averaged Navier-Stokes modeling of mixing layers, Phys. Rev. E **103**, 053108 (2021).

[22] J. R. Ristorcelli, Exact statistical results for binary mixing and reaction in variable density turbulence, Phys. Fluids **29**, 020705 (2017).

[23] A. W. Cook, W. Cabot, and P. L. Miller, The mixing transition in Rayleigh-Taylor instability, J. Fluid Mech. **511**, 333 (1999).

[24] W. H. Cabot and A. W. Cook, Reynolds number effects on Rayleigh-Taylor instability with possible implications for type Ia supernovae, Nat. Phys. **2**, 562 (2006).

[25] B. J. Olson and A. W. Cook, Rayleigh-Taylor shock waves, Phys. Fluids **19**, 128108 (2007).

[26] B. J. Olson, J. Larsson, S. K. Lele, and A. W. Cook, Non-linear effects of the combined Rayleigh-Taylor/Kelvin-Helmholtz instabilitiy, Phys. Fluids **23**, 114107 (2011).

[27] V. K. Tritschler, B. J. Olson, S. K. Lele, S. Hickel, X. Y. Hu, and N. A. Adams, On the Richtmyer-Meshkov instability evolving from a deterministic multimode planar interface, J. Fluid Mech. **755**, 429 (2014).

[28] B. J. Olson and J. Greenough, Large eddy simulation requirements for the Richtmyer-Meshkov instability, Phys. Fluids **26**, 044103 (2014).

[29] B. J. Olson and J. Greenough, Comparison of two- and three-dimensional simulations of miscible rychtmyer-meshkov instability with multimode initial conditions, Phys. Fluids **26**, 101702 (2014).

[30] B. E. Morgan, B. J. Olson, J. E. White, and J. A. McFarland, Self-similarity of a Rayleigh-Taylor mixing layer at low Atwood number with a multimode initial perturbation, J. Turbul. **18**, 973 (2017).

[31] A. Campos and B. E. Morgan, The effect of artificial bulk viscosity in simulations of forced compressible turbulence, J. Comput. Phys. **371**, 111 (2018).

[32] A. Campos and B. E. Morgan, Self-consistent feedbak mechanism for the sudden viscous dissipation of finite-mach-number compressing turbulence, Phys. Rev. E **99**, 013107 (2019).

[33] B. E. Morgan and W. J. Black, Parametric investigation of the transition to turbulence in Rayleigh-Taylor mixing, Physica D **402**, 132223 (2020).

[34] A. W. Cook, Artificial fluid properties for large-eddy simulation of compressible turbulent mixing, Phys. Fluids **19**, 055103 (2007).

[35] A. W. Cook, Enthalpy diffusion in multicomponent flows, Phys. Fluids **21**, 055109 (2009).

[36] R. W. Sharp and R. T. Barton, *HEMP Advection Model*, Report UCID 17809 (Lawrence Livermore Laboratory, Livermore, CA, 1981).

[37] R. M. Darlington, T. L. McAbee, and G. Rodrigue, A study of ALE simulations of Rayleigh-Taylor instability, Comput. Phys. Commun. **135**, 58 (2001).

[38] Tz. V. Kolev and R. N. Rieben, A tensor artificial viscosity using a finite element approach, J. Comput. Phys. **228**, 8336 (2009).

[39] M. J. Berger and J. Oliger, Adaptive mesh refinement for hyperbolic partial differential equations, J. Comput. Phys. **53**, 484 (1984).

[40] M. J. Berger and P. Colella, Local adaptive mesh refinement for shock hydrodynamics, J. Comput. Phys. **82**, 64 (1989).

[41] B. E. Morgan and J. A. Greenough, Large-eddy and unsteady RANS simulations of a shock-accelerated heavy gas cylinder, Shock Waves **26**, 355 (2016).

[42] K. S. Raman, O. A. Hurrican, H.-S. Park, B. A. Remington, H. Robey, V. A. Smalyuk, R. P. Drake, C. M. Krauland, C. c. Kuranz, J. F. Hansen, and E. C. Harding, Three-dimensional modeling and analysis of a high energy density Kelvin-Helmholtz experiment, Phys. Plasmas **19**, 092112 (2012).

[43] V. A. Smalyuk, M. Barrios, J. A. Caggiano, D. T. Casey, C. J. Cerjan, D. S. Clark, M. J. Edwards, J. A. Frenje, M. Gatu-Johnson, V. Y. Glebov, G. Grim, S. W. Haan, B. A. Hammel, A. Hamza, D. E. Hoover, W. W. Hsing, O. Hurrican, J. D. Kilkenny, J. L . Kline, J. P. Knauer *et al.*, Hydrodynamic instability growth and mix experiments at the National Ignition Facility, Phys. Plasmas **21**, 056301 (2014).

[44] S. V. Weber, D. T. Casey, D. C. Eder, J. D. Kilkenny, J. E. Pino, V. A. Smalyuk, G. P. Grim, B. A. Remington, D. P. Rowley, C. B. Yeamans, R. E. Tipton, M. Barrios, R. Benedetti, L. Berzak Hopkins, D. L. Bleuel, E. J. Bond, D. K. Bradley, J. A. Caggiano, D. A. Callahan, C. J. Cerjan *et al.*, Simulations of indirectly driven gas-filled capsules at the National Ignition Facility, Phys. Plasmas **21**, 112706 (2014).

[45] S. F. Khan, S. A. MacLaren, J. D. Salmonson, T. Ma, G. A. Kyrala, J. E. Pino, J. R. Rygg, J. E. Field, R. Tommasini, J. E. Ralph, D. P. Turbull, A. J. Kackinnon, K. L. Baker, L. R. Benedetti, D. K. Bradley, P. M. Celliers, E. L. Dewald, T. R. Dittrich, L. Berzak Hopkins, N. Izumi *et al.*, Symmetry tuning of a near one-dimensional 2-shock platform for code validation at the National Ignition Facility, Phys. Plasmas **23**, 042708 (2016).

[46] M. Gatu Johnson, A. B. Zylstra, A. Bacher, C. R. Brune, D. T. Casey, C. Forrest, H. W. Hermann, M. Hohenberger, D. B. Sayre, R. M. Bionta, J.-L. Bourgade, J. A. Caggiano, C. Cerjan, R. S. Craxton, D. Dearborn, M. Farrell, J. A. Frenje, E. M. Garcia, V. Yu. Glebov, G. Hale *et al.*, Development of an inertial confinement fusion platform to study charged-particle-producing nuclear reactions relevant to nuclar astrophysics, Phys. Plasmas **24**, 041407 (2017).

[47] M. Gatu Johnson, D. T. Casey, M. Hohenberger, A. B. Zylstra, A. Bacher, C. R. Brune, R. M. Bionta, R. S. Craxton, C. L. Ellison, M. Farrell, J. A. Frenje, W. Garbett, E. M. Garcia, G. P. Grim, E. Hartouni, R. Hatarik, H. W. Herrmann, M. Hohensee, D. M. Holunga, M. Hoppe *et al.*, Optimization of a high-yield, low-areal-density fusion product source at the National Ignition Facility with applications in nucleosynthesis experiments, Phys. Plasmas **25**, 056303 (2018).

[48] J. D. Bender, O. Schilling, K. S. Raman, R. A. Managan, B. J. Olson, S. R. Copeland, C. L. Ellison, D. J. Erskine, C. M. Huntington, B. E. Morgan, S. R. Nagel, S. T. Prisbrey, B. S. Pudliner, P. A. Sterne, C. E. Wehrenberg, and Y. Zhou, Simulation and flow physics of a shocked and reshocked high-energy-density mixing layer, J. Fluid Mech. **915**, A84 (2021).

[49] S. I. Warshaw, *The TDF System for Thermonuclear Plasma Reaction Rates, Mean Energies and Two-body Final State Particle Spectra*, Report UCRL-ID-144510 (Lawrence Livermore National Laboratory, Livermore, CA, 2001).

[50] E. G. Corman, W. E. Loewe, G. E. Cooper, and A. M. Winslow, Multigroup diffusion of energetic particles, Nucl. Fusion **15**, 377 (1975).

[51] H. Brysk, Electron-ion equilibration in a partially degenerate plasma, Plasma Phys. **16**, 927 (1974).

[52] R. M. More, K. H. Warren, D. A. Young, and G. B. Zimmerman, A new quotidian equation of state (QEOS) for hot dense matter, Phys. Fluids **31**, 3059 (1988).

[53] D. A. Young and E. M. Corey, A new global equation of state model for hot, dense matter, J. Appl. Phys. **78**, 3748 (1995).

[54] B. M. Haines, R. C. Shah, J. M. Smidt, B. J. Albright, T. Cardenas, M. R. Douglas, C. Forrest, V. Yu Glebov, M. A. Gunderson, C. E. Hamilton, K. C. Henderson, Y. Kim, M. N. Lee, T. J. Murphy, J. A. Oertel, R. E. Olson, B. M. Patterson, R. B. Randolph, and D. W. Schmidt, Observation of persistent species temperature separation in inertial confinement fusion mixtures, Nat. Commun. **11**, 544 (2020).

[55] R. E. Olson, T. J. Murphy, B. M. Haines, M. R. Douglas, B. J. Albright, M. A. Gunderson, Y. Kim, T. Cardenas, C. E. Hamilton, and R. B. Randolph, Development of the Marble experimental platform at the National Iginition Facility, Phys. Plasmas **27**, 102703 (2020).

[56] P. E. Dimotakis, The mixing transition in turbulent flows, J. Fluid Mech. **409**, 69 (2000).